

**Reaction products from high temperature treatments of**  
**(La<sub>x</sub>Gd<sub>1-x</sub>)<sub>2</sub>Zr<sub>2</sub>O<sub>7</sub> system and volcanic ashes powder mixtures**

Cynthia Y. Guijosa García <sup>1,4</sup>, Marco Antonio Rivera-Gil <sup>1,2</sup>, Chintalapalle V. Ramana <sup>3</sup>,  
Ravisankar Naraparaju <sup>4</sup>, Uwe Schulz <sup>4</sup>, Juan Muñoz-Saldaña <sup>1, a</sup>

<sup>1</sup> *Laboratorio Nacional de Proyección Térmica (CENAPROT), Centro de Investigación  
y de Estudios Avanzados del IPN, Libramiento Norponiente 2000 Fracc. Real de  
Juriquilla, 76230 Querétaro, Mexico*

<sup>2</sup> *Centro de Tecnología Avanzada, CIATEQ, Av. Manantiales 23A Parque Industrial  
Bernando Quintana, C.P. 76246, El Marqués, QRO, México.*

<sup>3</sup> *Department of Mechanical Engineering, University of Texas at El Paso, El Paso, TX  
79968, USA*

<sup>4</sup> *Institute of Materials Research, German Aerospace Center, Cologne 51147, Germany*

This version of the article has been accepted for publication, after peer review (when applicable) and is subject to Springer Nature's AM terms of use, but is not the Version of Record and does not reflect post-acceptance improvements, or any corrections. The

Version of Record is available online at: <http://dx.doi.org/>  
[\[https://doi.org/10.1007/s11837-022-05302-3\]](https://doi.org/10.1007/s11837-022-05302-3)

## Abstract

Rare-earth zirconate (REZ) pyrochlores, specifically  $(\text{La,Gd})_2\text{Zr}_2\text{O}_7$  are promising alternatives to substitute 7YSZ in thermal barrier coatings (TBC) due to their increased phase stability and resistance to calcium-magnesium-aluminosilicates (CMAS)-based damage at high temperatures. This work analyses the reaction products of isothermal treatments at 1250 °C of  $(\text{La}_x\text{Gd}_{1-x})_2\text{Zr}_2\text{O}_7$  powder mixtures in reaction with natural volcanic ashes (VAs) with different chemical compositions (Popocatepetl, Colima, and Eyjafjallajökull). The chemical composition in the  $(\text{La}_x\text{Gd}_{1-x})_2\text{Zr}_2\text{O}_7$  system showed a strong influence on the formation of reprecipitation products (Zr,Gd,La oxides), reactive crystallization products (La-Gd apatites, lanthanum silicates, zirconolite, and garnets), and intrinsic crystallization products (hematite-like structures). The formation of garnets, which enhance the mitigation effect against molten VAs/Si-deposits damage, was observed more promptly on  $(\text{La}_{0.5}\text{Gd}_{0.5})_2\text{ZrO}_7$  promoted by high contents of Fe, Ca, Ti, and Mg on VAs. Thus, the  $(\text{La}_{0.5}\text{Gd}_{0.5})_2\text{ZrO}_7$  system stands as a possible candidate to overcome today's threats for the integrity of current TBCs.

<sup>a</sup> Corresponding author: [jmunoz@cinvestav.mx](mailto:jmunoz@cinvestav.mx)

**Keywords:** TBC, rare-earth zirconates, pyrochlores, CMAS, volcanic ashes, reaction products.

## 1. Introduction

Thermal barrier coatings (TBCs) are widely used in the aeronautic industry to protect and thermochemically insulate metallic components of the hot section of turbine engines. Their use allows an increase in turbine's operation temperature thus leading to higher efficiency [1]. Nowadays, the most widely used material in such applications is zirconia stabilized with 6-8 wt.% of yttria, 7YSZ. 7YSZ's working temperature is restricted by the tetragonal  $\text{ZrO}_2$  (*t*-YSZ)  $\rightarrow$  monoclinic  $\text{ZrO}_2$  (*m*- $\text{ZrO}_2$ ) transformation at temperatures above 1200 °C and accelerated stabilization loss of the non-transformable tetragonal phase along with thermal cycling [2]. Such transformation is further accelerated by the presence of silica compounds such as those found in molten volcanic ashes, VAs [3] [4]. In addition, molten silica deposits infiltrate the open porosity of the coating to then solidify upon cooling generating residual stresses which can induce TBC failure [5] [6] [7]. This inhibits the lifetime of the coatings through the limitation of working temperature [5] [8] [9] [10]. In recent years, the constant volcanic activity around the world has increased these problems. For instance, flight paths through zones with high concentrations of suspended Si-based particles impose a safety threat for aircraft under certain working conditions [3] [11] [12]. One clear example was the eruption of the Eyjafjallajökull volcano in 2010 which affected air transportation all around Europe [4].

To study TBC degradation caused by molten silica deposits,  $\text{SiO}_2$ -based compounds matching the chemical composition of deposits found within failed aeronautic components. They have been synthetically reproduced in the laboratory. Such deposits, containing mostly Ca, Mg, Al, and Si are commonly known as CMAS [5] [13]. Additional replicas resembling the chemical composition of natural VAs, known as artificial volcanic ashes, AVAs have been synthesized and analyzed as well [13] [14] [15].

VAs and AVAs contain a wide number of elements including K, Na, Ti, Mn, Ca, Mg, Al, and Si. Comparing not only the elements but also their correspondent contents with the most reported CMAS, differences become clear. Among them, the Si content has significant differences comparing CMAS and VAs [10]. Such differences in chemical composition necessarily led to variations in thermal behavior.

In Mexico, there are currently two active volcanoes located in a high traffic air corridor (Colima and Popocatepetl) that show continuous and intense eruptive activity. Such activity constitutes a continuous source for airborne Si-based particles that can be ingested by engines, thus imposing a threat to the performance and lifetime of TBCs. To address risks associated with Si-based particles, the research of novel materials with enhanced thermochemical properties which can overcome 7YSZ limitations has been intensively pursuit. Such properties include phase stability at high temperatures which allows the increase of working temperature of turbine engines. For this, rare-earth zirconates, REZs, with the general formula  $\text{A}_2\text{Zr}_2\text{O}_7$  have been recently considered. Among REZs,  $\text{Gd}_2\text{Zr}_2\text{O}_7$  and  $\text{La}_2\text{Zr}_2\text{O}_7$  have drawn greater attention due to their phase stability above 1500 °C [16] [17]. When interacting with Si-based melts,  $\text{Gd}_2\text{Zr}_2\text{O}_7$  and  $\text{La}_2\text{Zr}_2\text{O}_7$  show the formation of reaction products with high Si- and Ca-content such as apatites  $\text{Ca}_2\text{RE}_8(\text{SiO}_4)_6\text{O}_2$  (RE=Gd, La) [10] [14] [15] [18]. The formation of such

apatites has been considered as a promising mitigation mechanism against infiltration and damage related to silica-based melts [14] [19] [20]. Furthermore, recent research indicates that Gd-La pyrochlores, known as lanthanum-gadolinium zirconate  $(\text{La}_x\text{Gd}_{1-x})_2\text{Zr}_2\text{O}_7$ , exhibit thermal stability beyond 1500 °C [16] [17]. Specifically, an improvement in thermal and mechanical properties has been reported for the  $x=0.5$  composition compared with the pure  $\text{La}_2\text{Zr}_2\text{O}_7$  or  $\text{Gd}_2\text{Zr}_2\text{O}_7$  systems [21]. Even with such promising properties for TBC applications, there is no reported data addressing the reactivity behavior after high temperature exposure of  $(\text{La}_{0.5}\text{Gd}_{0.5})_2\text{Zr}_2\text{O}_7$  interacting with VAs of Mexican active volcanoes.

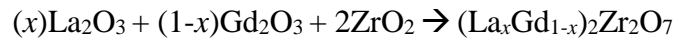
Thus, the main objective of this work is to study the reaction products generated by high temperature exposure of  $(\text{La}_x\text{Gd}_{1-x})_2\text{Zr}_2\text{O}_7$  powders mixed with high  $\text{SiO}_2$  VAs (77 and 80.7 mol% for Colima and Popocatepetl, respectively [3]) and to compare them with reaction products obtained by the interaction with VAs that contain lower  $\text{SiO}_2$  (57.9 mol% Eyjafjallajökull) and considerably higher contents of Fe and Ti (12.3 and 5.3 mol%, respectively).

The intrinsic thermal behavior of pure ashes is also studied to correlate VAs' properties with the formation of reaction products and to draw insights around the possible implications of the interaction of Si-based melts with actual La,Gd –based TBCs in terms of phase stability, infiltration, and damage.

## 2. Experimental Procedure

### 2.1 $(\text{La}_x\text{Gd}_{1-x})_2\text{Zr}_2\text{O}_7$ synthesis

$(\text{La}_x\text{Gd}_{1-x})_2\text{Zr}_2\text{O}_7$  ceramics with  $x$  content of 0, 0.5, and 1 were synthesized through mixed oxides and solid-state reaction assisted by mechanical milling from  $\text{ZrO}_2$ ,  $\text{Gd}_2\text{O}_3$ , and  $\text{La}_2\text{O}_3$  precursor oxides (Alfa Aesar, MA, USA) all of them having purities over 99%. Stoichiometric contents of the oxides were weighted following the equation



Stoichiometric mixtures for each  $x$  composition were then set inside alumina crucibles together with  $\text{ZrO}_2$  balls and ethanol as milling media. A fixed 10:1 balls to powder weight ratio was used for the milling. Reactants were processed in a planetary ball mill (Retsch PM 400, Haan, Germany) under a 250 rpm rotation speed for 3 h. Milled powders were dried using a hot plate at ~100 °C under magnetic stirring to remove ethanol.

Heat treatments consisting of 1450 °C for 7 h at a heating/cooling rates of 10 °C/min on air were performed in a tubular furnace (Yifan Furnace Co., Ltd., YFT1700, Henan, China) to promote the formation of the pyrochlore phases. Synthesized phases were hereafter identified as GZO, LGZO, and LZO for  $\text{Gd}_2\text{Zr}_2\text{O}_7$ ,  $(\text{La}_{0.5}\text{Gd}_{0.5})_2\text{Zr}_2\text{O}_7$ , and  $\text{La}_2\text{Zr}_2\text{O}_7$ , respectively. Characterization of the obtained systems was carried out by X-ray diffraction, XRD (Rigaku Corp, Tokyo, Japan) using a  $\text{CuK}_\alpha$  ( $\lambda = 1.5406 \text{ \AA}$ ) cathode operating at 30 kV and 20 mA. Measuring range was set between 20 and 65° in  $2\theta$ , with a 0.02° step size and 1°/min scan speed. Obtained diffractograms were analyzed by Rietveld refinement using GSAS to carry out lattice parameter calculations.

## 2.2 Volcanic ashes thermal behavior

For the experiments shown here, real VAs from Popocatepetl, Colima, and Eyjafjallajökull volcanoes corresponding to relatively recent eruptive events (2016, 2015, and 2010, respectively) were used. Mexican (Popocatepetl and Colima) and Iceland (Eyjafjallajökull) VAs were provided by the Geosciences department of UNAM and the Institute of Materials Research of the German Aerospace Center, respectively. The thermal behavior of the ashes was studied by differential scanning calorimetry, DSC (Setsys Evolution 16/18, Setaram, Caluire, France) under air, using powder samples of 14-55 mg and Pt crucibles. Measurements were performed from room temperature to 1450 °C with heating/cooling rate of 10 °C/min with a dwell time of 10 min at the maximum temperature followed by cooling to room temperature.

## 2.3 Effect of temperature on VAs phases content

Samples consisting of 1 g of as-received VAs were set on top of alumina substrates and heat treated at 1250 °C for 1 and 10 h under a heating/cooling rate of 10 °C/min using a conventional box furnace (Brother Furnace, XD-1700M, Zhengzhou, China). To study the first crystallization and microstructural changes, heat treated samples for 1 h were cross-sectioned and prepared for scanning electron microscopy (SEM), wavelength-dispersive X-ray spectroscopy (WDS), and chemical mapping measurements (JXA-8530F, JEOL, Tokyo, Japan) following standard metallographic techniques.

## 2.4 Volcanic ashes - $(\text{La}_x\text{Gd}_{1-x})_2\text{Zr}_2\text{O}_7$ powder mixtures

Powder mixtures of synthesized powders: VAs with a weight ratio of 60:40 were prepared by high-energy ball milling (SPEX 800D, Metuchen, NJ, USA) during 10 min at 1700 rpm using Nylamid crucibles and 10 mm zirconia balls in a dry milling media. Balls to powder: weight ratio used was 10:1. Considering the three ceramic systems and the three available VAs, a total of nine powder mixtures were processed. After the homogenization process, 0.5 g of each mixture was uniaxially pressed in a 10 mm-diameter tempered steel die under a 10 MPa pressure making use of standard hydraulic equipment. The obtained pellet mixtures were set on a Pt sheet and isothermally treated at 1250 °C for 1 and 10 h in the abovementioned box furnace using a heating/cooling rate of 10 °C/min. Interaction time and temperature were selected based on previous DSC analyses and corresponding TBCs' infiltration experiments reported for these ashes [3] which showed that at this temperature VAs are found within the melting range.

Heat treated pellets were mechanically removed from the Pt sheet and analyzed through XRD with the same conditions used for the analysis of the as-received VAs (section 2.1). After XRD analyses, the surfaces of the pellets were prepared following standard metallographic techniques and further measured through SEM and energy dispersive X-ray spectroscopy, EDS (XL30 ESEM-EDS, Philips, Eindhoven, The Netherlands). EDS analyses consisted of at least three spot measurements of chemical composition, performed on each of the discernible microstructures within the samples. Additional to the polished samples, for the 1 h heat treated pellets, a replica was inspected through SEM without metallographic preparation to analyze the as-treated surface morphology.

### 3. Results

#### 3.1 Synthesis of the $(\text{La}_x\text{Gd}_{1-x})_2\text{Zr}_2\text{O}_7$ ceramic systems

Fig. 1 shows typical results of structural analysis of the synthesized powders. XRD diffraction patterns of the  $(\text{La}_x\text{Gd}_{1-x})_2\text{Zr}_2\text{O}_7$  systems are shown in Fig. 1a, where no secondary phases are observed. Pyrochlore diffraction peaks around 29, 34, 48, and 61.5°, corresponding to the (222), (400), (440) and (444) planes, respectively were observed. The super-lattice reflections around ~14, 37, and 43° in 2 $\theta$ , corresponding to the (111), (331), and (511) diffraction peaks, respectively [22] [23] confirmed the pyrochlore phase. It is well known, that the intensity of these peaks is related to their structure order degree [24], which is proportional to the La content in the  $(\text{La}_x\text{Gd}_{1-x})_2\text{Zr}_2\text{O}_7$  system meaning that in the case of GZO, such intensities are rather weak. This experimental fact agrees with previous literature reports regarding the degree of order-disorder in  $\text{A}_2\text{B}_2\text{O}_7$  pyrochlores [22] [23], where the order degree is given by the ratio between the average cationic radii of the species occupying the A and B positions ( $r_A/r_B$ ) [25]. The corresponding lattice parameters of the prepared ceramics determined by Rietveld analysis of the XRD patterns are shown in Fig. 1b. A linear increase of the lattice parameter with the La content is observed. This behavior is consistent with the theoretical values reported for GZO and LZO pyrochlore structures [26] that fits Vegard's law indicating the formation of a solid solution [21] [22] [23]. Additionally, the increase in the lattice parameter is related to the shift of the (622) diffraction peak ~58° to lower values on 2 $\theta$  which implies higher interplanar distances that may be further related to changes in the lattice due to substitutions on the A site. Therefore, these results suggest a successful substitution of  $\text{Gd}^{3+}$  by  $\text{La}^{3+}$  during the formation of the solid solution for  $0 < x < 1$  values of the  $(\text{La}_x\text{Gd}_{1-x})_2\text{Zr}_2\text{O}_7$  system [21].

#### 3.2 Volcanic Ashes

##### 3.2.1 Chemical composition

The chemical composition of VAs used in these experiments has been previously reported elsewhere [3] and summarized in Table I, where the broad range of oxide contents that exist among the VAs is highlighted.  $\text{SiO}_2$  content shows the greater chemical difference, which ranges from 57.9 mol% for Eyjafjallajökull to 77 and 80.7 mol% for Colima and Popocatepetl, respectively. Additionally, the  $\text{FeO}_x$  content shows great variations being 12.3 mol% for Eyjafjallajökull and 4.1 and 3.6 mol% for Colima and Popocatepetl, respectively.  $\text{CaO}$ ,  $\text{TiO}_2$ , and Al variations are also seen.  $\text{SiO}_2$ ,  $\text{FeO}_x$ ,  $\text{CaO}$ , and  $\text{TiO}_2$  contents are related to the infiltration kinetics due to the reaction products [9] [15] [18].

##### 3.2.2 Structural behavior

XRD diffraction patterns of the as-received and of the 1 and 10 h heat treated VAs are also reported in the literature [3]. As-received VAs contain up to 57 % mol of  $\text{SiO}_2$  which contributes to the amorphous phase. Among crystalline phases identified were quartz ( $\text{SiO}_2$ , Q), albite ( $\text{NaAlSi}_3\text{O}_8$ , Ab), and orthoclase ( $\text{KAlSi}_3\text{O}_8$ , Or), anorthite ( $\text{CaAl}_2\text{Si}_2\text{O}_8$ , An) and iron oxide ( $\text{Fe}_2\text{O}_3$ , H) in the diffraction peaks of the three as-received VAs [13] [27].

After 1 and 10 h of heat treatments, Mexican VAs become in amorphous state and only A peak remains visible. On the other hand, Eyjafjallajökull VAs are transformed into a partially crystalline state with the heat treatment where ilmenite ( $\text{FeTiO}_3$ , Im) combined with Ab, An, and Q phases were previously identified [3].

### 3.2.3 Thermal behavior

DSC cooling curves for the three VAs are shown in Fig. 2. The corresponding heating curves were previously reported elsewhere [3] where the glass transition temperatures,  $T_g$  of Popocatepetl and Colima (750 °C) were found to be around 50 °C higher than Eyjafjallajökull VAs. The corresponding melting ranges were reported as 900–1100 °C, 1060–1200 °C, and 1035–1150 °C for Popocatepetl, Colima and Eyjafjallajökull, respectively. DSC cooling curves of VAs with a high content of  $\text{SiO}_2$  (Colima and Popocatepetl) can be approximated to a linear trend with no additional exothermic or endothermic peaks. Linear approximations have been attributed to systems containing high amounts of amorphous phases [13]. Nevertheless, for the Eyjafjallajökull VA the exothermic peak observed at 953 °C can be related to the crystallization of the ilmenite phase ( $\text{FeTiO}_3$ , Im) which may take place upon cooling. This result is in accordance with similar systems reported elsewhere [3] [28]. Differences in thermal behavior among tested VAs are indicators of the crystallization and thermal dependence of the ashes with chemical composition and phase contents being of special relevance to those related to Ca, Fe, and Ti. Finally, the cooling curves behavior suggests an intrinsic crystallization in Fe-rich VAs.

According to this information, the testing temperature to follow the ceramic-VA interaction experiments is set to 1250 °C, corresponding to the melting range of the VAs and also matching common temperatures in turbine engines [3].

### 3.2.4 Effect of heat treatment on the microstructural changes of VAs

Cross-section micrographs of VAs samples heat treated for 1 h at 1250 °C are shown in Fig. 3 along with corresponding chemical mappings. In general, the microstructure of the three VAs consists of a Si-based glass matrix with differences in chemical contents of Al, Fe, Ca, Mg, K, and Na as expected from chemical analyses of the as-received ashes [3]. For the three samples, the formation of needle-like microstructures is observed. According to EDS analysis, such needles predominantly contain Si and Al with low contents of Ca as shown in Table II. The growth of such microstructure begins at the glass/substrate interface, which suggests their formation as a product of the high temperature reactivity of the Si-based melts with  $\text{Al}_2\text{O}_3$  which has been described in the literature [29].

In addition, VAs from Popocatepetl and Colima show cluster-shaped structures with high content of Ca surrounded by the needle-like structures as shown in Fig. 3. The chemical composition of these microstructures measured through EDS is also shown in Table III. From chemical mapping and SEM/EDS measurements and according to what was observed in XRD, such cluster-like structures correspond to sodian anorthite ( $\text{NaCaAl}_2\text{Si}_2\text{O}_8$ ) [3], indicated as An in Fig. 3a, b.

In Eyjafjallajökull VAs, Fe,Ti-rich crystals with prismatic microstructure are associated with ilmenite and homogeneously distributed in the volume of the material (Fig. 3c). In addition to Fe and Ti,  $Mg^{2+}$  cations substituting  $Fe^{2+}$  leading to the formation of magnesian-ilmenite  $(Fe,Mg)TiO_3$  [30] have been reported. It is worth mentioning that the absence of ilmenite crystals in the Popocatepetl and Colima VAs is attributed to their low content of Fe and Ti (Table I).

### 3.3 Reaction products

XRD diffraction patterns of the VAs- $(Gd_xLa_{1-x})_2Zr_2O_7$  mixtures, heat treated at 1250 °C for 1 and 10 h are shown in Fig. 4. In this figure, the patterns in a, b, and c columns correspond to mixtures of the three VAs with GZO, LGZO and LZO ceramic powders, respectively. XRD patterns of pure GZO, LGZO, and LZO powders are also given as references. As previously discussed, all the mixtures exhibit a contribution of amorphous phases which can be related to the particular characteristics of the ashes and their behavior after heat treatments. For the identification of phases, the information not only from XRD patterns but complemented with the SEM microstructures of samples heat treated for 1 and 10 h (Fig. 5 and Fig. 6) and composition obtained with EDS analysis were used. Based on these results the interactions of the  $(Gd_xLa_{1-x})_2Zr_2O_7$  systems with VAs are summarized as follows.

#### 3.3.1 VAs-GZO interactions

Fig. 4a, d show XRD diffraction patterns of interactions of GZO with VAs for 1 and 10 h at 1250 °C. Cubic zirconia,  $c\text{-}ZrO_2$  (ICDD 49-1642) was identified in all mixtures with the (111) and (200) diffraction peaks around  $\sim 30$  and  $34^\circ$  in  $2\theta$ , respectively. In the micrographs recorded after 1 h of heat treatment (Fig. 5a-c) cubic zirconia was identified as globular shaped precipitates. Increasing the heat treatment time to 10 h these precipitates increase in size keeping their content constant (Fig. 6a-c). The identification of  $c\text{-}ZrO_2$  was confirmed with the EDS analysis of globular precipitates (**Error! Reference source not found.**), where the presence of Gd was measured and represented as an oxide-normalized content between 15 and 8 % of  $Gd_2O_3$ . For samples after 1 h interactions, the  $Gd_2O_3$  content in the globular precipitates is lower in the Eyjafjallajökull-GZO mixtures than in mixtures with Si-rich VAs (Colima and Popocatepetl). On the other hand, for 10 h heat treatments,  $Gd_2O_3$  contents in the  $c\text{-}ZrO_2$ -type phases show a tendency to decrease with  $SiO_2$  content from the ashes. This behavior is consistent with interactions of GZO with Si-rich CMAS reported in the literature [18].

Additionally, gadolinium-apatite phase,  $Ca_2Gd_8(SiO_4)_6O_2$ ,  $Ap_{Gd}$ , (ICDD 28-0212) was identified through its (210), (211), and (112) main peaks in the range of  $29$  to  $32^\circ$ . Characteristic hexagonal morphology of the apatite crystals was observed; however, due to the metallographic treatment, they appear as needle shaped grains in the SEM micrographs (Fig. 5 and Fig. 6). The chemical composition of such apatites indicates that as expected, they are rich in Si and Gd, with an approximation to the RE-apatite general formula  $Ca_2RE_8(SiO_4)_6O_2$  with Al and Zr minor contents. It has been reported that for AVAs-REZ pyrochlore interactions, the chemical composition of such apatites presents Al and Zr substitutions when AVAs have a chemical composition similar to that from



Eyjafjallajökull [14]. Therefore, this behavior suggests the formation of RE-apatites with Al, Zr substitutions.

Interactions with Fe-rich VAs (Eyjafjallajökull) also show the presence of zirconolite  $\text{CaZrTi}_2\text{O}_7$ , ZC, and hematite-like structures,  $\text{Fe}_2\text{O}_3$ , H, for 1 and 10 h of heat treatments (Fig. 5c and Fig. 6c).

Zirconolite crystals (ZC) were confirmed through EDS and SEM analysis. Such crystals contain 50.89 Zr, 16.95 Gd, and 14.95 Fe at.% with additional contents of 13.84 Ti, 3.37 Al, and <2 Si at.%. Additionally, the characteristic peaks of zirconolite  $\sim 30, 35, 50^\circ$  were identified through XRD; however, these peaks may also match the position of the *c*- $\text{ZrO}_2$  phase. The presence of zirconolite is inferred from the widening of the *c*- $\text{ZrO}_2$  peaks (Fig. 4a, d) instead of the presence of individually defined peaks for each crystalline phase.

EDS chemical analysis of the Fe-rich hematite-like phase shown as prismatic microstructures (Fig. 7) indicates that such structures contain Mg, Al, Ti, and Zr (Table V), from which Mg, Al, and Zr at. % in hematite-like grains increases with heat treatment time, while the Ti and Fe tend to decrease. A similar behavior is reported in the literature for interactions of REZ with AVAs [14].

### 3.3.2 VAs-LGZO interactions

Tetragonal zirconia, *t*- $\text{ZrO}_2$  (ICDD 50-1089) was identified with its main peaks around  $30.2, 34.8, 35.2,$  and  $50.3^\circ$  (Fig. 4b, e) which correspond to the (011), (002), (110), and (112) diffraction peaks, respectively. However, intensity changes due to the increase of heat treatment time are mostly noticed by the intensity decrease of the *t*- $\text{ZrO}_2$  main peak ( $30.3^\circ$ ) and the increase of the monoclinic  $\text{ZrO}_2$  related peak around  $28.1^\circ$  (ICDD 86-1451). Globular shaped grains (Fig. 5d-f and Fig. 6d-f) with sizes between 300-500 nm were identified. However, due to the reduced size of the precipitates reliable EDS point measurements were not possible. Nevertheless, it has been reported that such fine microstructure matches with *t*- $\text{ZrO}_2$  [18] which is in agreement with XRD results. For both testing times (1 and 10 h) twined structures are observed, which are characteristic of the *t*- $\text{ZrO}_2 \rightarrow m$ - $\text{ZrO}_2$  phase transformation [18] [19]. Due to this observation and XRD analysis, the presence of *t,m*- $\text{ZrO}_2$  phases is confirmed.

Additionally, La-Gd apatite phase ( $\text{Ap}_{\text{LaGd}}$ ) was identified in the XRD patterns. However, to the best author's knowledge, no diffraction file is available for the identification of this phase. Nevertheless, the main peaks located in  $30.07$  and  $31.77^\circ$  corresponding to the (112) and (211) planes of  $\text{Ap}_{\text{Gd}}$  and  $\text{Ap}_{\text{La}}$ , respectively [31] [32] (Fig. 4b, e) were taken as a reference for its classification as a La-Gd-apatite, provided that, according to the literature, RE-apatites show peaks that shifts to lower angles with increasing RE cation sizes [31] [32]. Regardless of the known partial overlapping of  $\text{Ap}_{\text{LaGd}}$  with (111) *m*- $\text{ZrO}_2$  pattern the identification of this phase can be confirmed with EDS analysis (Table IV) which showed La and Gd contents that allows proposing the  $\text{Ca}_2(\text{Gd}_{1-y}\text{La}_y)_8(\text{SiO}_4)_6\text{O}_2$  general formula of the  $\text{Ap}_{\text{LaGd}}$  as a result of LGZO-VA interactions.

Hematite,  $\text{Fe}_2\text{O}_3$ , and  $\text{A}_3\text{B}_2\text{Z}_3\text{O}_{12}$  garnet-like microstructures denoted as H and G in Fig. 5f and Fig. 6f, respectively were observed in the  $(\text{La}_x\text{Gd}_{1-x})_2\text{Zr}_2\text{O}_7$  interactions with the

Fe-rich VA for both heat treatments. The chemical composition of hematite-like structures showed contents of Mg, Al, Si, Ti, Fe, and Zr. Additionally, <2 at.% of La and Gd were detected. In contrast with GZO-interaction shown in 3.3.1, Gd was not detected within the hematite-like structure. Si, Ti, and Zr contents showed an increasing tendency for 10 h heat treatment (**Error! Reference source not found.**). Whereas, Mg, Al, La, Gd, and Fe showed a decreasing trend.

Garnet-like, microstructures, denoted as G in Fig. 5f and Fig. 6f showed high content of Si and La according to the chemical composition by EDS analysis. Also, Mg, Al, Ca, Ti, Fe, Zr, and Gd are observed (Table VI). The presence of apatites and ZrO<sub>2</sub> agglomerates together with the formation of garnets were observed (Fig. 8b). Reported studies of interactions of Fe,-Ti-rich CMAS with 7YSZ have shown the formation of the specific kimzeyite garnet (Ca<sub>3</sub>(Zr,Ti,Fe)<sub>2</sub>(Al,Fe,Si)<sub>3</sub>O<sub>12</sub>), containing Zr as one of the main constituents [9]. From the SEM and EDS analyses conducted here, and following the possible garnet cationic substitutions discussed by Braue *et al.* [9], the feasible formation of RE-based garnets with different stoichiometries for each ceramic system are proposed in Table VI. In this study and due to the high content of La detected, these structures are here called RE-garnets. Additionally, in Fig. 8b a cohesion of garnets and apatites is observed, generating an apparent sealing layer on the surface of these products.

### 3.3.3 VAs-LZO interactions

Tetragonal and monoclinic zirconia were identified through their correspondent main peaks (011) and (-111) at 30.1° and 28.1°, respectively (Fig. 4c, f). Additionally, between 34 and 36° two wide peaks are observed which may be related to the (002) and (110) diffraction peaks of the *t*-ZrO<sub>2</sub> overlapping with the (002), (020), and (200) *m*-ZrO<sub>2</sub> planes. In the range of 28-30° peaks related to the tetragonal phase decrease in intensity with time, whereas the intensity of the monoclinic-related peaks increases instead. Characteristic microstructural features associated with ZrO<sub>2</sub> are observed in Fig. 5g-i and Fig. 6g-i. The corresponding chemical composition is shown in Table III. ZrO<sub>2</sub> microstructures exhibit La<sub>2</sub>O<sub>3</sub> contents below 5 mol% for Si-rich VAs (Popocatepetl and Colima). According to the literature, this content of La<sub>2</sub>O<sub>3</sub> in zirconia can be related to the formation of the *t*-ZrO<sub>2</sub> [33]. However, for all 10 h interactions La<sub>2</sub>O<sub>3</sub> decreases to values below 2 mol% which can be related to *m*-ZrO<sub>2</sub> solid solution [33]. In contrast, for 1 h this behavior is only seen in the interaction with Fe-rich VAs (Eyjafjallajökull). Such observations are also consistent with observations made through XRD. Finally, for both testing times (1 and 10 h) twined structures related to the *t*-ZrO<sub>2</sub>→*m*-ZrO<sub>2</sub> phase transformation can be barely seen due to resolution SEM limitations, which are similar to those previously reported by TEM [14] [15] [18] [19].

La-apatite with the stoichiometry Ca<sub>2</sub>La<sub>8</sub>(SiO<sub>4</sub>)<sub>6</sub>O<sub>2</sub> (ICDD 29-0337) identified as Ap<sub>La</sub> was observed by XRD patterns with its main peaks located between 28 and 32°, corresponding to the (210), (112) and (300) (Fig. 4c, f). As depicted by SEM/EDS micrographs, its hexagonal morphology presents a chemical composition of Si, Ca, and La with contents of Zr and Al as observed in Table IV and Fig. 5g-i and Fig. 6g-i. In the literature, the presence of Al has not been yet reported for Ap<sub>La</sub>. However, the high

solubility of  $\text{Al}_2\text{O}_3$  in lanthanum silicates is known [34], thus suggesting the possibility of its presence.

Lanthanum silicate,  $\text{La}_2\text{Si}_2\text{O}_7$ , LS was observed with a diffraction peak  $\sim 26^\circ$ , that corresponds to the (021) plane of the  $\text{La}_2\text{Si}_2\text{O}_7$  (ICDD 48-0052) (Fig. 4c, f). LS was only observed in the interaction of LGZO powder with Colima ashes. Hexagonal crystals with comparatively greater size than that from apatites ( $>5\ \mu\text{m}$  compared to  $<3\ \mu\text{m}$ ) can be related to LS not only through morphological features but also through chemical composition analysis (Fig. 5h and Fig. 6h). From EDS analysis (Table VII) it can be seen that these crystals are Si-La-rich with low contents of Zr. The LS microstructure is observed around the globular-shaped  $\text{ZrO}_2$  crystals which can also help to explain the Zr-enrichment of the LS phase. Comparing 1 and 10 h heat treatments it can be seen that the Si, La, and Zr contents decrease with increasing heat treatment time, which may indicate the possibility of further reactions to form additional phases if longer times were applied.

For the interactions with Fe-rich ashes (Eyjafjallajökull) microstructures associated with the phases hematite, H, and garnet, G, were identified for heat treatment of 1 and 10 h (Fig. 5g-i and Fig. 6g-i). On the other hand, Fig. 8a, c shows the hematite and garnet microstructure on the surface of this interaction. In such micrographs, hematite and garnet show larger sizes in comparison with microstructures observed in LGZO interaction (Fig. 8b). Hematite and garnet-like phases grow along with  $\text{ZrO}_2$  and apatite. This behavior is possibly associated with the Zr and Al presence in the H and G phases, as observed in form their chemical composition (Table V and Table VI, respectively). Additionally, cracks are observed on the surfaces which can be related to volume changes due to the growth of reaction products with large sizes such as garnets (Fig. 8c).

The proposed structures here are based on EDS, SEM, and XRD results and supported by information published in the literature. However, additional characterization techniques such as TEM is required to confirm the formation of phases that are very small in size and could not be identified by the aforementioned techniques.

### 3.4 Si-based glass matrix after chemical interaction

Si-based glass matrices were identified in all samples. EDS analysis of these matrices (not shown here) indicated the presence of Al, Mg, Na, Zr, Gd, and La with traces of K, Ca, Ti, and Fe. Moreover, An can be found within the formed glass matrix as it has been reported in the literature for most CMAS compositions [18]. However, XRD measurements performed in this work do not show the presence of An, Ab or Q (Fig. 4). Also, needle-like structures which have been related to the presence of An [29] were not detected within the glass matrix. This fact represents an additional difference RE-zirconates interacting with  $\text{SiO}_2$ -rich CMAS compared to natural VAs in the glass matrix characteristics.

A semi-quantitative estimation of the area fraction corresponding to the glass-matrix was performed by image analysis in the recorded micrographs. The results of area fraction corresponding to the glass for GZO, LGZO, and LZO interactions is given in Fig. 9 for 1 and 10 h heat treatment, which allows evaluating the effect of the chemical composition

of VAs. As a result, VAs containing high  $\text{FeO}_x$  (Eyjafjallajökull) show lower glass area fraction than  $\text{FeO}_x$ -poor ashes (Colima and Popocatepetl). This result matches with those obtained from XRD and SEM/EDS analysis, where it was determined that products are promoted by the Fe and Ti contents in VAs. Moreover, a higher glass matrix fraction is formed with increasing heat-treatment time (Fig. 9b). However, more work has to be done to study the reaction kinetics as a function of time, testing interaction times (e.g. 20, 50, 100, 200 h) similar to what has been reported for CMAS [8] [11] [18]. About the effect of the composition of the RE-zirconates, the  $x=0.5$  composition, LGZO shows the lowest proportion of glass matrix (Fig. 9). Meanwhile, only for the LZO ( $x=0$ ), the glass matrix increases with the content of  $\text{SiO}_2$  in the tested VAs.

#### 4. Discussion

From the obtained results, the formation of several reaction products through the high temperature interactions of  $(\text{Gd}_x\text{La}_{1-x})_2\text{Zr}_2\text{O}_7$  with VAs was confirmed. Their formation does not depend exclusively on the chemical composition of the VAs, but also on the nature of the ceramic system. In this work, the high temperature reactivity of ashes from Popocatepetl, Colima, and Eyjafjallajökull volcanoes with three RE-zirconates namely GZO, LGZO, and LZO was evaluated. These materials have been pinpointed as promising candidates against infiltration and chemical degradation of TBCs caused by molten  $\text{SiO}_2$ -based compounds such as VAs and CMAS [20] [21].

##### 4.1 Characteristics of VAs deposits before chemical interactions

The volcanic ashes used in this work show structural, microstructural, and chemical differences between each other. Such differences can be attributed to a wide range of variables such as the geographic location of their source (central Mexico for Colima and Popocatepetl, and southwest Iceland for Eyjafjallajökull) as well as the meteorological conditions at the moment of the eruptive activity and the intrinsic characteristics of such volcanic activity [3] [4] [11].

The crystallization changes produced by heat treatments of the pure as-received ashes were studied and observations drawn from this work agree with what has been previously reported in the literature [3]. Regarding the VAs' microstructure, for the first crystallization stages (evaluated after 1 h of heat treatment), the influence of the as-received chemical composition can be observed. For instance, the formation of Fe,-Ti-rich crystals is seen to be formed in the interactions with Fe-rich ashes Eyjafjallajökull, whereas for Fe-poor ashes no such crystals were identified. In contrast for Fe-poor ashes, Ca containing anorthite crystals are formed (Fig. 4).

Strong chemical and structural differences between natural and artificial volcanic ashes, as well as CMAS have been reported elsewhere [3] [11]. Most studies of the interaction between TBCs and airborne particles are mainly based on CMAS. However, the current results contribute to highlight the importance of studying the interactions of  $(\text{La}_x\text{Gd}_{1-x})_2\text{Zr}_2\text{O}_7$  with specific VAs, especially considering that  $\text{SiO}_2$  content of VAs can go as high as 80 mol% compared to the common contents found on synthetic CMAS, which is around 45 mol% [11] [19].

## 4.2 Reactivity of $(\text{La}_x\text{Gd}_{1-x})_2\text{Zr}_2\text{O}_7$ with VAs

The identified reaction products from the high temperature interactions of RE-pyrochlores with VAs are summarized and showed schematically in in Fig. 10. Such reaction products were broadly classified as a) reprecipitation reaction, b) intrinsic crystallization and c) reactive crystallization products [18]. This classification is given based on the nature of their crystallization process and will be discussed as follows.

### 4.2.1 Reprecipitation reaction products

Reprecipitation reaction products are among the first reaction products to be formed during the heat treatments and are promoted by the presence of  $\text{ZrO}_2$ , which in turn is generated from the dissolution of  $(\text{La}_x\text{Gd}_{1-x})_2\text{Zr}_2\text{O}_7$  by the action of  $\text{SiO}_2$ -based melts. Such dissolutions lead to the formation of RE-Zr oxides with different stoichiometry from the original  $(\text{La}_x\text{Gd}_{1-x})_2\text{Zr}_2\text{O}_7$ . It has been reported that different  $\text{ZrO}_2$  polymorphs namely *t*- $\text{ZrO}_2$ , *m*- $\text{ZrO}_2$ , and *c*- $\text{ZrO}_2$  can form solid solutions with RE cations through the pyrochlore dissolution. Each of the zirconia polymorphs can dissolve different amounts of RE. For example, it has been reported that *t*- $\text{ZrO}_2$  can dissolve up to 5 mol% of  $\text{RE}_2\text{O}_3$ , whereas *m*- $\text{ZrO}_2$  can dissolve up to 2 mol%, and *c*- $\text{ZrO}_2$ , usually referred to as fluorite defective zirconia (*f*- $\text{ZrO}_2$ ), can dissolve up to 80 mol% of RE oxide within its structure [33]. For this, zirconia-based RE solid solutions are commonly expressed in terms of  $\text{RE}_2\text{O}_3$  and  $\text{ZrO}_2$  contents.

Zirconia polymorphs precipitated from the interaction with Si-rich VAs show higher  $\text{RE}_2\text{O}_3$  molar percentage than Fe-rich VAs (Table III). For Colima, Popocatepetl and Eyjafjallajökull these contents are 11.2, 15.6 and 9.7 mol%, respectively when interacting with GZO for 1 h, and tending to increase with time. This result suggests that GZO and LZO have both high solubility with Si-rich VAs, being the latter the highest one. Similar behavior is expected for the LGZO.

According to this and from XRD and EDS results, it seems that *c*- $\text{ZrO}_2$  is formed by the interaction of GZO with either of the tested VAs. Meanwhile for the interactions of La-containing systems, LGZO and LZO, the presence of *t*- $\text{ZrO}_2$  and *m*- $\text{ZrO}_2$  is observed. Thus, it can be inferred that the *c*- $\text{ZrO}_2 \rightarrow t$ - $\text{ZrO}_2 \rightarrow m$ - $\text{ZrO}_2$  phase transformations are promoted by the increase of La in the ceramic and it also increases with heat treatment time.  $\text{RE}_2\text{O}_3$  containing *c*- $\text{ZrO}_2$ , *t*- $\text{ZrO}_2$ , and *m*- $\text{ZrO}_2$  phases constitute reprecipitation reaction products.

Provided that cubic and tetragonal phases of zirconia have been identified in the literature as a key to the effective reactive crystallization between TBC ceramic such as GZO, LZO and molten silicates [18] [19]. In this work this effect is confirmed for the tested compositions of the  $(\text{La}_x\text{Gd}_{1-x})_2\text{Zr}_2\text{O}_7$  system as well.

### 4.2.2 Intrinsic reaction products

Intrinsic crystallization products consist of phases that contain elements that are only found within the glass matrix [18]. Results of AVAs infiltration on GZO and LZO TBCs that show the formation of Fe-rich phases have been reported elsewhere [8] [14]. Such

phases include hematite ( $\text{Fe}_2\text{O}_3$ ) with contents of Mg and Ti and fayalite ( $\text{Fe}_2\text{SiO}_4$ ) with contents of Mg and Al for GZO and LZO interactions, respectively [14] [15].

In this work Fe-rich phases with low contents of Zr, La, and/or Gd were detected. These products correspond to the microstructures identified as hematite, occurring only for the interactions with Fe-rich ashes (Eyjafjallajökull). Also, hematite shows Si-enrichment, thus suggesting their reaction with Si from the melt.

As seen in Fig. 3, for the heat treatments of pure ashes, Fe,-Ti crystals consisting of ilmenite nucleate and grow homogeneously dispersed in the silica matrix. Such phases can transform into mellite,  $(\text{Ca})_2(\text{Al,Mg})(\text{Al,Si})\text{SiO}_7$ , spinel,  $\text{MgAl}_2\text{O}_7$ , or even garnets,  $\text{X}_3\text{Y}(\text{Fe})_2\text{Z}(\text{Fe})_3\text{O}_{12}$ . Analogously, for the interaction of the VAs with the ceramic systems, Fe and Ti could serve as nucleation points for the formation of the  $(\text{Fe,Mg})\text{TiO}_2$ -type phases which could later transform into more complex reaction products such as Fe-garnets.

### 4.2.3 Reactive crystallization products

Reactive crystallization products are phases constituted by elements from the VAs and the RE-pyrochlores [18]. Among them, the formation of apatites (Ap), lanthanum silicate (LS), zirconolite (ZC), and RE-garnets (G) were identified as reaction products.

In the case of the  $\text{Ca}_2\text{RE}_8(\text{SiO}_4)_6\text{O}_2$  ( $\text{Ap}_{\text{RE}}$ ), the formation of  $\text{Ap}_{\text{Gd}}$  and  $\text{Ap}_{\text{La}}$  were identified from the reactions of GZO and LZO with VAs. Additionally, the  $\text{RE}^{3+}$  position in the general apatite formula can be occupied by La and/or Gd [31] [32] leading to the possible formation of a complex  $\text{Ca}_2(\text{La,Gd})_8(\text{SiO}_4)_6\text{O}_2$  apatite ( $\text{Ap}_{\text{GdLa}}$ ) from the interaction of La,-Gd-zirconate with VAs.

The chemical composition of  $\text{Ap}_{\text{Gd}}$ ,  $\text{Ap}_{\text{La}}$ , and  $\text{Ap}_{\text{GdLa}}$ , shown in (Table IV) reveals the presence of Al and Zr. This suggests additional cationic substitutions in the general apatite structure. To describe such substitutions a model based in the effective ionic radii of substituting cations in  $\text{Ap}_{\text{Gd}}$  has been proposed [15]. Such a model considers the substitution of the  $\text{Si}^{4+}$  (0.26 Å) tetrahedral sites by  $\text{Al}^{3+}$  (0.39 Å). On the other hand,  $\text{Gd}^{3+}$  (1.0 Å) can be substituted by  $\text{Zr}^{4+}$  (0.78 Å). Finally,  $\text{La}^{3+}$  (1.1 Å) can also substitute  $\text{Gd}^{3+}$  to produce the complex  $\text{Ap}_{\text{GdLa}}$  [14] [15] [31].

For the apatites formed through the interaction of RE-ceramics with VAs containing high  $\text{SiO}_2$  and low  $\text{CaO}$ , the amount of Al and Zr substitutions is higher. In addition to such substitutions and due to the low contents of Ca available for the apatite formation, additional occupancy of Gd and La in Ca position is also plausible considering the effective ionic radii of  $\text{Gd}^{3+}$ ,  $\text{La}^{3+}$ , and  $\text{Ca}^{2+}$  [15].

On the other hand, an opposite behavior is seen for the apatites formed from VAs with high contents of  $\text{FeO}_x$  and  $\text{CaO}$ . In general, as Si, Ca, Gd, and La, increase and Al and Zr contents is decreased, apatites approximate to the general apatite  $\text{Ca}_2\text{RE}_8(\text{SiO}_4)_6\text{O}_2$  with low cationic substitutions. According to the current results, the formation of a solid solution Gd,-La apatite,  $\text{Ap}_{\text{GdLa}}$ , can be expected for the high temperature interaction of VAs with  $(\text{La}_x\text{Gd}_{1-x})_2\text{Zr}_2\text{O}_7$  in the  $0 < x < 1$  range.

On the other hand, except for LZO-Colima, the interactions of ceramics with a high content of SiO<sub>2</sub> show the formation of apatites and ZrO<sub>2</sub>-based phases as reaction products. In contrast, only the LZO-Colima interaction exhibits the formation of La<sub>2</sub>Si<sub>2</sub>O<sub>7</sub>, LS, in addition to apatites and ZrO<sub>2</sub>-based structures. The formation of LS has been related in the literature to the high contents of SiO<sub>2</sub> in the ashes [14]. However, this phase was not detected in the interactions with Popocatepetl, even when SiO<sub>2</sub> content in such ashes is slightly higher than in Colima VAs. This further suggests a difference in high temperature behavior that may go beyond the elemental composition of the ashes.

Considering the effective ionic radii for Si<sup>4+</sup> (0.26 Å), La<sup>3+</sup> (1.1 Å), and Zr<sup>4+</sup> (0.78 Å), as well as the substitutional model for RE-silicates reported in the literature [15], the substitution of La<sup>3+</sup> by Zr<sup>4+</sup> in La<sub>2</sub>Si<sub>2</sub>O<sub>7</sub> is here proposed leading to the possible formation of a lanthanum-zirconium silicate, (La,Zr)<sub>2</sub>Si<sub>2</sub>O<sub>7</sub>, with the stoichiometry given in Table VII. Additionally, no evidence of stoichiometry variation with time can be seen from these data.

The effect of the presence of (La,Zr)<sub>2</sub>Si<sub>2</sub>O<sub>7</sub> on the infiltration process is not known yet. However, it is believed that the reaction process involving La, Zr, and Si, may help to reduce infiltration kinetics if the process takes place in a TBC. To corroborate this, further studies are needed in TBC systems.

On the other hand, through the interactions of RE-pyrochlores with Fe-rich VAs, a wider variety of reaction products have been detected. Specifically, for GZO interactions the zirconolite phase is formed. As observed in Fig. 7, zirconolite is a reaction product growing from the globular ZrO<sub>2</sub> as well as hematite crystals. According to their morphology and growth, they can be related to secondary reaction products grown at the expense of primary products such as the globular zirconia crystals and hematite. From the general stoichiometry of zirconolite, CaZrTi<sub>2</sub>O<sub>7</sub>, cationic substitutions of Gd<sup>3+</sup> and Fe<sup>3+</sup> by Ca<sup>2+</sup> and Ti<sup>4+</sup> have been reported elsewhere [15]. From this, and in addition to the chemical composition reported here, the specific Gd<sub>0.68</sub>Zr<sub>2.04</sub>Fe<sub>0.6</sub>Ti<sub>0.55</sub>Al<sub>0.13</sub>O<sub>7</sub> RE-zirconolite stoichiometry is proposed as a reaction product of GZO-VAs interactions. Furthermore, within the zirconolite structure, low Si contents were detected suggesting further reactions which may lead to the formation of additional products such as RE-garnets, especially for long periods (>10 h).

As another reactive crystallization product, RE-garnets were identified for the La-containing systems, LGZO and LZO. Garnet stoichiometric formula is A<sub>3</sub>B<sub>2</sub>Z<sub>3</sub>O<sub>12</sub>, where Ca<sup>2+</sup> and Mg<sup>2+</sup> occupy the A site, whereas the B site is usually occupied by Zr<sup>2+</sup>, Ti<sup>4+</sup>, and Fe<sup>2+</sup>. Also, based on reported observations of Y<sup>3+</sup> occupancy of the B position [9] [11], it seems that the B site can also be occupied by RE<sup>3+</sup> such as Gd<sup>3+</sup> and/or La<sup>3+</sup>. Finally, the Z position can be occupied by Al<sup>3+</sup>, Fe<sup>3+</sup>, and Si<sup>4+</sup> [9] [11]. From the reported formation of Gd-garnets with Gd<sup>3+</sup> in the A site, the proposed stoichiometry corresponding to Gd<sub>3</sub>Sc<sub>2</sub>Ga<sub>3</sub>O<sub>12</sub> opens the possibility for the Gd<sup>3+</sup> to occupy the A site [35]. The garnet stoichiometry proposed in this work is based on such observations (Table VI).



The wide variety of possible stoichiometry variations involved in the formation of RE-garnets evidences that garnets are complex solid solutions that can show a wide variety of cationic substitutions in different positions of the structure [9] [18].

It has been reported that the formation of such garnets is favored by low cooling rate [19], such as in the case of the experiments conducted in this work (10 °C/min). Also, garnets exhibit a comparatively big morphology that increases in volume as it grows from apatite crystals and ZrO<sub>2</sub> agglomerates (Fig. 8b, c). This observation suggests that a garnet formation is given as a secondary reaction product formed from apatites and zirconia. This increase in size and volume may generate additional stresses within the ceramic which at some point could also compromise the integrity of the system when used for TBC's applications [19]. However, garnets capture great amounts of silica from the melt thus changing the infiltration kinetics, which in turn could act as a mitigation mechanism form CMAS infiltration during the turbine's operation [11] [36].

The formation of La-Gd-containing garnets has not been published before in the literature and the study of their formation addressing reaction mechanisms, stability, mechanical and thermal properties would help to the understanding and design of future TBCs based on RE-pyrochlores. Tailored chemical composition of such advanced TBCs could then show enhanced chemical stability and infiltration resistance against high temperature infiltration and chemical interaction with SiO<sub>2</sub>-based melts.

Evidence shown here indicate that among the studied VAs, those with a high content of Fe have an increased capability to destabilize La,-Gd zirconates, compared to Fe-poor VAs. Also, Fe content in the ashes has seen to better promote nucleation points for the growth of crystalline phases [13] compared with Fe-poor ashes [3] [18] [28]. On the other hand, the diversity of phases formed from the interactions of La-based pyrochlores with VAs illustrates the high reactivity of La-ceramics compared to other RE-based systems such as GZO and LGZO.

### **4.3 Implications for TBC systems**

The 7YSZ degradation in the presence of CMAS, AVAs, and VAs melts is broadly described and studied in the literature [3] [5] [8]. In all cases, authors agree that such interactions result in the rapid degradation of the TBC ceramic by both thermochemical and physical mechanisms.

On the other hand, RE-zirconates have shown better performance against Si-melts [14] [20]. However, the performance of La-Gd solid solutions, LGZO, as TBC and ceramics against CMAS/VAs melts has not been published.

When comparing the effect of the variation of the RE-pyrochlore ceramic composition, similar behavior in terms of the formation of reaction products was observed among the tested systems. However, when evaluating the effect of the chemical composition of SiO<sub>2</sub>-based sources (VAs), significant differences in reaction products were seen.

It is well known that there are great differences between the chemical composition of natural sources such as VAs, sands, and fly sash, with laboratory synthesized CMAS [10]. Among them, the content of SiO<sub>2</sub> can vary by up to 30 mol% and nearly by 20 mol% for



$\text{FeO}_x$ . As shown in this work, the effect of iron oxide, whose effect is usually neglected in the literature plays a preponderant roll in chemical degradation of RE-pyrochlores and possibly on the infiltration behavior of TBCs based on such materials. This is related to the influence exerted by Fe on the reaction kinetics. In addition,  $\text{SiO}_2$  is among the most influential oxides on viscosity, surface tension, and thermal behavior of  $\text{SiO}_2$ -based melts and thus, great differences are expected for the different melts.

In addition to the characteristics of the Si deposits, the nature of ceramics used as protective coatings is of paramount importance for TBC's performance. These reasons motivate the study of high temperature interactions of novel ceramics, such as complex RE-pyrochlores, with  $\text{SiO}_2$ -based sources containing comparatively higher contents of silica, such as VAs. From these studies, it is also suggested that in addition to the chemical composition of the VAs, the phase content of the as-received Si-based samples may influence the formation of reaction products and thus, the ceramic's performance against  $\text{SiO}_2$  melts.

By the use of three natural sources of VAs and three RE-ceramic systems, the research presented here has confirmed that reaction products are influenced by both TBC and Si-melt characteristics. Studies were carried out in powder mixtures containing 60 wt.% of ceramic and 40 wt.% of VA which is considered to be higher than the usually reported value of (20  $\text{mg}/\text{cm}^2$ ) reported for coatings' testing [15]. With the use high-energy milling homogenization of the mixtures, the distribution and high surface area available for reactions was promoted. As such, obtained results may help depict high temperature interactions of  $(\text{La}_x\text{Gd}_{1-x})_2\text{Zr}_2\text{O}_7$  TBCs with melts showing  $\text{SiO}_2$  and  $\text{FeO}_x$  variation under extreme time and concentration conditions.

LGZO,  $x=0.5$  composition showed promising behavior against VAs attack due to the formation of RE-apatite and RE-garnet where they consume most of the cations and leaves very less residue. Reports about  $(\text{La}_x\text{Gd}_{1-x})_2\text{Zr}_2\text{O}_7$  as TBC have not been found in the literature, although this system seems to have the potential to significantly improve the performance of TBCs due to their thermal stability at 1500 °C (that leads to a high sintering resistance) and a thermal conductivity lower than YSZ, which is even lower than GZO (2.1 W/mK) and LZO (1.8 W/mK) [16] [17]. Furthermore, the sintering resistance to LGZO can be used to design a porous microstructure in a coating favoring further reduction in thermal conductivity and compensating stresses generated by the mismatch in the coefficients of thermal expansion of TBC (LGZO) and the metallic substrate. However, it is known that the thermo-mechanical properties of RE-zirconates are poor compared to YSZ. Efforts to increase the fracture toughness of the  $(\text{La}_x\text{Gd}_{1-x})_2\text{Zr}_2\text{O}_7$  system are needed [21].

Solving the brittleness problem and combining the favorable thermal properties with the effective crystallization of the apatite and garnet phases against the attack of molten silicates makes the LGZO system a potentially promising material to be used as TBC. Therefore, studies of infiltration resistance, mechanical properties, and thermal stability experiments e.g. plasma sprayed TBCs are currently on-going.

## 5. Conclusions

Pyrochlore ceramic powders of the  $(\text{La}_x\text{Gd}_{1-x})_2\text{Zr}_2\text{O}_7$  system with compositions of  $x = 0$ , 0.5, and 1 were synthesized through the solid-state reaction of mixed oxides showing a linear trend in the variation of lattice parameter as a function of Gd/La content. Intrinsic crystallization of ashes from Popocatepetl, Colima and Eyjafjallajökull volcanoes depends strongly on its chemical composition, where Fe-rich VAs crystallize the ilmenite phase while Si-rich VAs the anorthite phase. In the latter case Ca plays an important role in the crystallization stage. Reaction products between ceramics powders and VAs were evaluated by powder mix and interactions during 1 and 10 h at 1250 °C.  $\text{ZrO}_2$ -phases with considerable La or Gd contents as dissolution products from the pyrochlore phase showed the following relationship  $c\text{-ZrO}_2 \rightarrow t\text{-ZrO}_2 \rightarrow m\text{-ZrO}_2$  as a function of La content and time. Apatite of La, La-Gd, and Gd were identified in all reactions. Interactions with Si-rich VAs and LZO lead to the formation of La-silicate as a secondary reaction product. Fe-rich VAs form hematite phases as an intrinsic primary product, as well as zirconolite and garnet as a reactive secondary product. LZO show higher reactivity with Fe-rich VAs. LGZO has shown the formation of  $\text{ZrO}_2$ -base, apatite, La-Gd garnet phases as the main reaction products. In addition to the fact that the LGZO exhibits the lower thermal conductivity and Young's modulus than either of GZO and LZO, current study indicates that its resistance against siliceous melts is also much better than LZO and GZO. Based on its lower thermal conductivity and high temperature phase stability LGZO can be proposed as a candidate material for TBC applications, however, realization as coatings still imposes many hurdles with respect to processing difficulties. Once these issues are solved, thermal cyclic life time and sintering issues must be analyzed as well.

## Acknowledgements

The authors thank the Mexican Council for Science and Technology, CONACYT for funding related to this project (293429). Also, thanks to Dr. L. Capra from the Geosciences department of UNAM for providing the Colima and Popocatepetl ashes. J. Muñoz-Saldaña thanks to CONACYT and the Alexander von Humboldt Foundation for financial support for research activities at the German Aerospace Center, DLR. This work has been carried out jointly at CENAPROT and LIDTRA national laboratories in Mexico and the High-Temperature and Functional Coatings department of DLR in Germany. CVR acknowledges, with pleasure, support from the National Science Foundation (NSF) with NSF-PREM grant #DMR-1827745.

## Conflict of interest

Authors declare no personal or financial conflicts of interest.

## References

1. D.R. Clarke, M. Oechsner and N.P. Padture, *MRS Bulletin*, 37, 891-898 (2012). <https://doi.org/10.1557/mrs.2012.232>
2. A.G. Evans, D.R. Clarke and C.G. Levi, *Journal of the European Ceramic Society*, 28, 1405-1419 (2008). <https://doi.org/10.1016/j.jeurceramsoc.2007.12.023>
3. M.A. Rivera-Gil, J.J. Gomez-Chavez, C.V. Ramana, R. Naraparaju, U. Schulz and J. Muñoz-Saldaña, *Surface and Coatings Technology*, 378, 124915 (2019). <https://doi.org/10.1016/j.surfcoat.2019.124915>
4. W.R. Chen and L.R. Zhao, *Procedia Engineering*, 99, 795-803 (2015). <https://doi.org/10.1016/j.proeng.2014.12.604>
5. C.G. Levi, J.W. Hutchinson, M.-H. Vidal-Sétif and C.A. Johnson, *MRS Bulletin*, 37, 932-941 (2012). <https://doi.org/10.1557/mrs.2012.230>
6. R. Naraparaju, M. Huttermann, U. Schulz and P. Mechnich, *Journal of the European Ceramic Society*, 37, 261-270 (2017). <https://doi.org/10.1016/j.jeurceramsoc.2016.07.027>
7. R. Naraparaju, U. Schulz, P. Mechnich, P. Dobber and F. Seidel, *Surf Coat Tech*, 260, 73-81 (2014). <https://doi.org/10.1016/j.surfcoat.2014.08.079>
8. P. Mechnich, W. Braue and U. Schulz, *Journal of the American Ceramic Society*, 94, 925-931 (2011). <https://doi.org/10.1111/j.1551-2916.2010.04166.x>
9. W. Braue, P. Mechnich and D.J. Green, *Journal of the American Ceramic Society*, 94, 4483-4489 (2011). <https://doi.org/10.1111/j.1551-2916.2011.04747.x>
10. D.L. Poerschke, R.W. Jackson and C.G. Levi, *Annual Review of Materials Research*, 47, 297-330 (2017). <https://doi.org/10.1146/annurev-matsci-010917-105000>
11. R. Naraparaju, J.J. Gomez Chavez, U. Schulz and C.V. Ramana, *Acta Materialia*, 136, 164-180 (2017). <https://doi.org/10.1016/j.actamat.2017.06.055>
12. W. Song, S. Yang, M. Fukumoto, Y. Lavallée, S. Lokachari, H. Guo, Y. You and D.B. Dingwell, *Acta Materialia*, 171, 119-131 (2019). <https://doi.org/10.1016/j.actamat.2019.04.011>
13. E.M. Zaleski, C. Ensslen, C.G. Levi and D. Butt, *Journal of the American Ceramic Society*, 98, 1642-1649 (2015). <https://doi.org/10.1111/jace.13478>
14. U. Schulz and W. Braue, *Surface and Coatings Technology*, 235, 165-173 (2013). <https://doi.org/10.1016/j.surfcoat.2013.07.029>
15. P. Mechnich, W. Braue and D.J. Green, *Journal of the American Ceramic Society*, 96, 1958-1965 (2013). <https://doi.org/10.1111/jace.12251>
16. M. Stopyra, I. Saenko, M. Ilatovskaia, G. Savinykh and O. Fabrichnaya, *Journal of the American Ceramic Society*, 102, 7628-7644 (2019). <https://doi.org/10.1111/jace.16613>
17. D. Shin, H.-G. Shin and H. Lee, *Calphad*, 45, 27-32 (2014). <https://doi.org/10.1016/j.calphad.2013.11.002>
18. D.L. Poerschke, T.L. Barth and C.G. Levi, *Acta Materialia*, 120, 302-314 (2016). <https://doi.org/10.1016/j.actamat.2016.08.077>
19. D.L. Poerschke and C.G. Levi, *Journal of the European Ceramic Society*, 35, 681-691 (2015). <https://doi.org/10.1016/j.jeurceramsoc.2014.09.006>
20. S. Krämer, J. Yang and C.G. Levi, *Journal of the American Ceramic Society*, 91, 576-583 (2008). <https://doi.org/10.1111/j.1551-2916.2007.02175.x>

21. C.L. Wan, W. Pan, Q. Xu, Y.X. Qin, J.D. Wang, Z.X. Qu and M.H. Fang, *Physical Review B*, 74, 144109 (2006). <https://doi.org/10.1103/PhysRevB.74.144109>
22. C. Wan, Z. Qu, A. Du and W. Pan, *Acta Materialia*, 57, 4782-4789 (2009). <https://doi.org/10.1016/j.actamat.2009.06.040>
23. L. Fan, X. Shu, X. Lu, Y. Xie, Y. Ding, T. Duan, B. Dang and Y. Wu, *Ceramics International*, 41, 11741-11747 (2015). <https://doi.org/10.1016/j.ceramint.2015.05.140>
24. X.W. J. Wu, N. P. Padture, P. G. Klemens, M. Gell, E. Garcia, P. Miranzo, M. I. Osendi, *American Ceramic Society*, 85, 3031-3035 (2002).
25. Z. Wang, G. Zhou, X. Qin, F. Zhang, J. Ai, P. Liu and S. Wang, *Journal of the European Ceramic Society*, 34, 3951-3958 (2014). <https://doi.org/10.1016/j.jeurceramsoc.2014.05.046>
26. M. A. Subramanian, A.W. Sleight, *Rare Earth Pyrochlores*, ed. K.A. Gschneidner, Jr. and L. Eyring (Elsevier, USA, 1993), p. 225-248. [https://doi.org/10.1016/S0168-1273\(05\)80018-2](https://doi.org/10.1016/S0168-1273(05)80018-2).
27. T.J. Casadevall, *U.S. Geological Survey Bulletin*, 2047, 87-92 1994. <https://doi.org/10.3133/b2047>
28. R. Naraparaju, H. Lau, M. Lange, C. Fischer, D. Kramer, U. Schulz and K. Weber, *Surface and Coatings Technology*, 337, 198-208 (2018). <https://doi.org/10.1016/j.surfcoat.2018.01.030>
29. M.H. Vidal-Sétif, C. Rio, D. Boivin and O. Lavigne, *Surface and Coatings Technology*, 239, 41-48 (2014). <https://doi.org/10.1016/j.surfcoat.2013.11.014>
30. A.K. Temple, *Economic Geology*, 61, 695-714 (1966).
31. J.V. Crum, S. Chong, J.A. Peterson and B.J. Riley, *Acta Crystallogr E Crystallogr Commun*, 75, 1020-1025 (2019). <https://doi.org/10.1107/S2056989019008442>
32. F. Perrudin, C. Rio, M.H. Vidal-Sétif, C. Petitjean, P.J. Panteix and M. Vilasi, *Journal of the European Ceramic Society*, 37, 2657-2665 (2017). <https://doi.org/10.1016/j.jeurceramsoc.2017.02.022>
33. E.R. Andrievskaya, *Journal of the European Ceramic Society*, 28, 2363-2388 (2008). <https://doi.org/10.1016/j.jeurceramsoc.2008.01.009>
34. H.J.S. U. Kolitsch, F. Aldinger, *Journal of Phase Equilibria*, 19, 426-433 (1998).
35. T. Shintaku, A. Tate and S. Mino, *Applied Physics Letters*, 71, 1640-1642 (1997). <https://doi.org/10.1063/1.120003>
36. J.J.G. Chavez, R. Naraparaju, C. Mikulla, P. Mechnich, K. Kelm, C.V. Ramana and U. Schulz, *Corrosion Science*, 190, 109660 (2021). <https://doi.org/10.1016/j.corsci.2021.109660>

### Figure captions

Fig. 1. a) XRD patterns of the synthesized  $\text{Gd}_2\text{Zr}_2\text{O}_7$ ,  $(\text{La}_{0.5}\text{Gd}_{0.5})_2\text{Zr}_2\text{O}_7$  and  $\text{La}_2\text{Zr}_2\text{O}_7$  systems showing corresponding characteristic peaks, b) linear fit for lattice parameters indicating the formation of a solid solution. Lattice parameters were calculated using Rietveld refinement of XRD patterns.

Fig. 2. DSC cooling curves for as-received Popocatepetl, Colima, and Eyjafjallajökull VAs. Figure were obtained using a heating/cooling rate of  $10\text{ }^\circ\text{C}/\text{min}$ .

Fig. 3. SEM images showing microstructural features and EDS chemical mapping of a) Popocatepetl, b) Colima, and c) Eyjafjallajökull VAs. These micrographs correspond to thermal treatments consisting of 1 h dwell at  $1250\text{ }^\circ\text{C}$  using a heating/cooling rate of  $10\text{ }^\circ\text{C}/\text{min}$ .

Fig. 4. XRD patterns of the 1 and 10 h interactions at  $1250\text{ }^\circ\text{C}$  of a,d) Popocatepetl, b,e) Colima and c,f) Eyjafjallajökull with  $\text{Gd}_2\text{Zr}_2\text{O}_7$ ,  $(\text{La}_{0.5}\text{Gd}_{0.5})_2\text{Zr}_2\text{O}_7$ , and  $\text{La}_2\text{Zr}_2\text{O}_7$  ceramics.

Fig. 5. SEM micrographs of the reaction products formed at  $1250\text{ }^\circ\text{C}$  for 1 h-interactions between GZO (a,b,c), LGZO (d,e,f), LZO (g,h,i) and Popocatepetl, Colima and Eyjafjallajökull ashes. Where  $\text{Ap}_{\text{RE}}$  is apatite of La and/or Gd, H is hematite, G is garnet, ZC is zirconolite, and LS is lanthanum silicate.

Fig. 6. SEM micrographs of the reaction products formed at  $1250\text{ }^\circ\text{C}$  for 10 h interactions between GZO (a,b,c), LGZO (d,e,f), LZO (g,h,i) systems and Popocatepetl, Colima and Eyjafjallajökull ashes. Where  $\text{Ap}_{\text{RE}}$  is apatite of La and/or Gd, H is hematite, G is garnet, ZC is zirconolite, and LS is lanthanum silicate.

Fig. 7. SEM micrograph the interaction of GZO-Eyjafjallajökull VA for 1 h. In the micrograph the formation of zirconolite is designed as ZC.

Fig. 8. SEM surface micrographs (without metallographic preparation) for mixtures of Eyjafjallajökull ashes with LZO (a) and c)), LGZO (b)) heat-treated at  $1250\text{ }^\circ\text{C}$  during 1 h. Microstructures corresponding to the Fe-rich phases (H), garnets (G), apatites (Ap), and  $\text{ZrO}_2$  phases (Z).

Fig. 9. Plots of the area fraction (%) corresponding to glass matrix for all ceramic – VA mixtures, heat treated for a) 1 h and b) 10 h at  $1250\text{ }^\circ\text{C}$ . Measurements were performed by using the software ImageJ for SEM surface micrographs.

Fig. 10. Summary of reaction products formed through the interactions  $(\text{La}_x\text{Gd}_{1-x})_2\text{Zr}_2\text{O}_7$  system and volcanic ashes.

## Tables

Table I. Chemical composition of studied ashes as reported by Rivera *et al.* [3].

Source	mol%							
	SiO <sub>2</sub>	TiO <sub>2</sub>	Al <sub>2</sub> O <sub>3</sub>	FeO <sub>T</sub>	MgO	CaO	Na <sub>2</sub> O	K <sub>2</sub> O
Popocatepetl	80.7	1.3	2.1	3.6	0.1	3.2	8.0	0.18
Colima	77.0	0.8	4.3	4.1	0.3	5.6	7.9	0.16
Eyjafjallajökull	57.9	5.3	5.6	12.3	3.1	11.5	4.5	0.15

Table II. Chemical composition (at.%) of Ca-rich grains, measured through EDS. POP= Popocatepetl, COL= Colima and EYJ= Eyjafjallajökull. \*Std. Deviation < 0.6 at.%.

VA/ Element	Glass			Needles			An		Im	
	POP	COL	EYJ	POP	COL	EYJ	POP	COL	EYJ	
	(at.%)									
Si	51.8	54.3	44.4	48.5	57.6	49.5	44.9	45.4	-	
Al	17.8	18.2	15.2	27.9	23.0	26.4	31.5	30.9	-	
Na	2.1	2.2	3.0	10.4	9.6	9.6	8.1	9.0	-	
Ca	7.3	5.7	19.3	13.0	9.6	14.3	15.5	14.5	-	
Mg	5.1	4.3	4.7	-	-	-	-	-	-	11.1
K	5.7	6.0	2.4	-	-	-	-	-	-	-
Fe	8.4	8.0	7.1	-	-	-	-	-	-	74.4
Ti	1.3	0.9	3.6	-	-	-	-	-	-	14.3

Table III. Chemical composition (at.%) of globular morphologies shown in Figure 6 and Figure 7, measured through EDS. \*Std. deviation < 3 mol.%.

System	Time (h)	Phase	ZrO <sub>2</sub>	Gd <sub>2</sub> O <sub>3</sub>	La <sub>2</sub> O <sub>3</sub>
			(mol%)		
GZO+POP	1	<i>c</i> -ZrO <sub>2</sub>	88.8	11.2	-
GZO+COL	1	<i>c</i> -ZrO <sub>2</sub>	84.4	15.6	-
GZO+EYJ	1	<i>c</i> -ZrO <sub>2</sub>	90.3	9.7	-
GZO+POP	10	<i>c</i> -ZrO <sub>2</sub>	91.5	8.5	-
GZO+COL	10	<i>c</i> -ZrO <sub>2</sub>	91.1	8.9	-
GZO+EYJ	10	<i>c</i> -ZrO <sub>2</sub>	90.4	9.6	-
LZO+POP	1	<i>t</i> -ZrO <sub>2</sub>	97.4	-	2.6
LZO+COL	1	<i>t</i> -ZrO <sub>2</sub>	94.4	-	4.3
LZO+EYJ	1	<i>m</i> -ZrO <sub>2</sub>	98.5	-	1.5
LZO+POP	10	<i>m</i> -ZrO <sub>2</sub>	98.7	-	1.3
LZO+COL	10	<i>m</i> -ZrO <sub>2</sub>	99.7	-	0.3
LZO+EYJ	10	<i>m</i> -ZrO <sub>2</sub>	99.5	-	0.5

Table IV. Chemical composition of apatite crystals measured through EDS (at.%). \*Std. deviation < 5 at.%.

System	Time (h)	Ca <sup>2+</sup>	Si <sup>4+</sup>	Al <sup>3+</sup>	Zr <sup>4+</sup>	Gd <sup>3+</sup>	La <sup>3+</sup>
		(at.%)					
Theoretical apatite Ca <sub>2</sub> (RE,RE') <sub>8</sub> Si <sub>6</sub> O <sub>26</sub>		12.5	37.5	-	-	50.0-y	y
GZO+POP	1	9.4	26.7	10.8	23.0	30.1	-
GZO+COL	1	7.2	28.4	9.1	20.4	34.9	-
GZO+EYJ	1	11.8	33.2	4.3	3.8	47.0	-
GZO+POP	10	10.3	31.8	5.7	4.7	47.6	-
GZO+COL	10	8.7	30.3	7.2	12.2	41.6	-
GZO+EYJ	10	13.9	32.3	5.2	1.4	47.1	-
LGZO+POP	1	9.5	29.4	8.1	16.6	21.5	14.9
LGZO+COL	1	8.5	28.7	8.8	19.0	20.5	14.4
LGZO+EYJ	1	12.8	32.2	5.3	9.9	24.5	15.3
LGZO+POP	10	3.2	31.0	6.5	8.4	32.0	18.9
LGZO+COL	10	9.0	30.5	7.0	16.6	21.7	15.1
LGZO+EYJ	10	13.4	32.3	5.2	5.6	27.1	16.5
LZO+POP	1	11.3	29.8	7.7	12.7	-	38.5
LZO+COL	1	11.0	28.1	9.4	17.1	-	34.5
LZO+EYJ	1	13.9	31.2	6.3	17.0	-	31.6
LZO+POP	10	11.0	29.5	8.0	10.1	-	41.4
LZO+COL	10	11.9	33.0	4.5	6.3	-	44.3
LZO+EYJ	10	14.0	31.8	5.7	3.7	-	44.8

Table V. Chemical composition of *H* crystals measured through EDS (at.%). \*Std. deviation < 3 at.%.

System	Time (h)	Mg	Al	Si	Ti	Fe	Zr	Gd	La
		(at.%)							
GZO+EYJ	1	5.5	8.2	6.3	3.2	75.4	1.2	-	-
	10	14.9	11.7	16.9	1.4	41.5	7.9	-	-
LGZO+EYJ	1	26.4	16.3	4.7	0.2	43.7	4.8	1.5	1.5
	10	15.1	12.0	15.1	1.4	41.5	10.4	0.8	0.8
LZO+EYJ	1	22.7	15.1	5.8	-	51.0	1.6	-	3.5
	10	30.6	18.5	0.3	-	46.2	4.1	-	-

Table VI. Chemical composition of RE-garnet structures measured through EDS (at.%).

\*Std. deviation < 2 at.%.

System	Time (h)	Mg	Al	Si	Ca	Ti	Fe	Zr	La	Gd	Proposed stoichiometry
(at.%)											
LGZO	1 h	4.2	8.4	27.8	2.9	7.3	10.7	18.0	13.5	6.8	$(\text{Ca}_{0.4}\text{Mg}_{0.6})_3(\text{Zr}_{0.4}\text{Ti}_{0.2}\text{La}_{0.3}\text{Gd}_{0.1})_2(\text{Al}_{0.2}\text{Fe}_{0.2}\text{Si}_{0.6})_3\text{O}_7$
LGZO	10 h	4.1	9.0	29.9	2.5	7.8	13.8	10.9	15.2	6.4	$(\text{Ca}_{0.4}\text{Mg}_{0.6})_3(\text{Zr}_{0.3}\text{Ti}_{0.2}\text{La}_{0.4}\text{Gd}_{0.2})_2(\text{Al}_{0.2}\text{Fe}_{0.3}\text{Si}_{0.6})_3\text{O}_7$
LZO	1 h	2.9	9.2	30.0	2.1	10.5	14.6	7.0	23.4	-	$(\text{Ca}_{0.4}\text{Mg}_{0.6})_3(\text{Zr}_{0.2}\text{Ti}_{0.3}\text{La}_{0.6})_2(\text{Al}_{0.2}\text{Fe}_{0.3}\text{Si}_{0.6})_3\text{O}_7$
LZO	10 h	4.4	11.7	38.4	0.8	-	10.6	6.7	27.0	-	$(\text{Ca}_{0.2}\text{Mg}_{0.8})_3(\text{Zr}_{0.2}\text{La}_{0.8})_2(\text{Al}_{0.2}\text{Fe}_{0.2}\text{Si}_{0.6})_3\text{O}_7$

Table VII. Chemical composition for lanthanum silicates, measured through EDS (at.%).

\*Std. deviation < 4 at.%.

System	Time (h)	Si	Zr	La	Proposed stoichiometry
(at.%)					
LZO+COL	1	16.3	5.64	11.99	$\text{Si}_2(\text{La}_{0.68}\text{Zr}_{0.32})_2\text{O}_7$
LZO+COL	10	15.7	4.6	10.46	$\text{Si}_2(\text{La}_{0.69}\text{Zr}_{0.31})_2\text{O}_7$



## Figures

Figure 1.

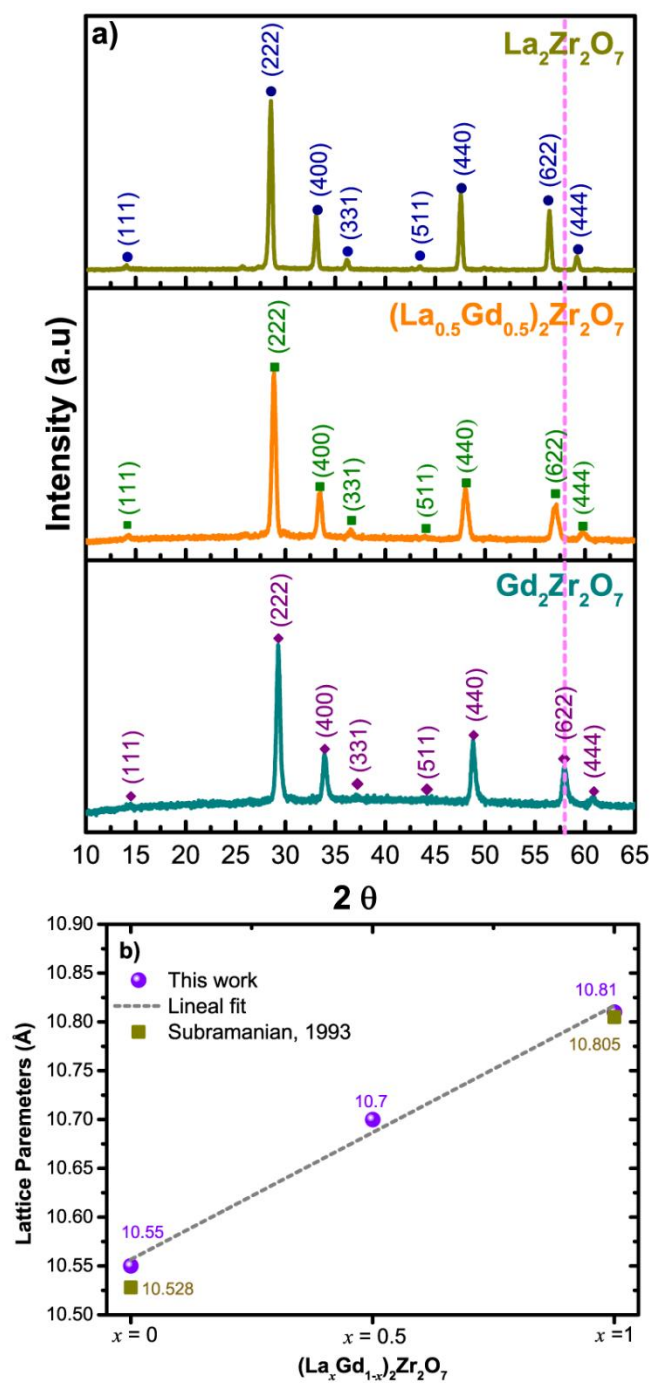


Figure 2.

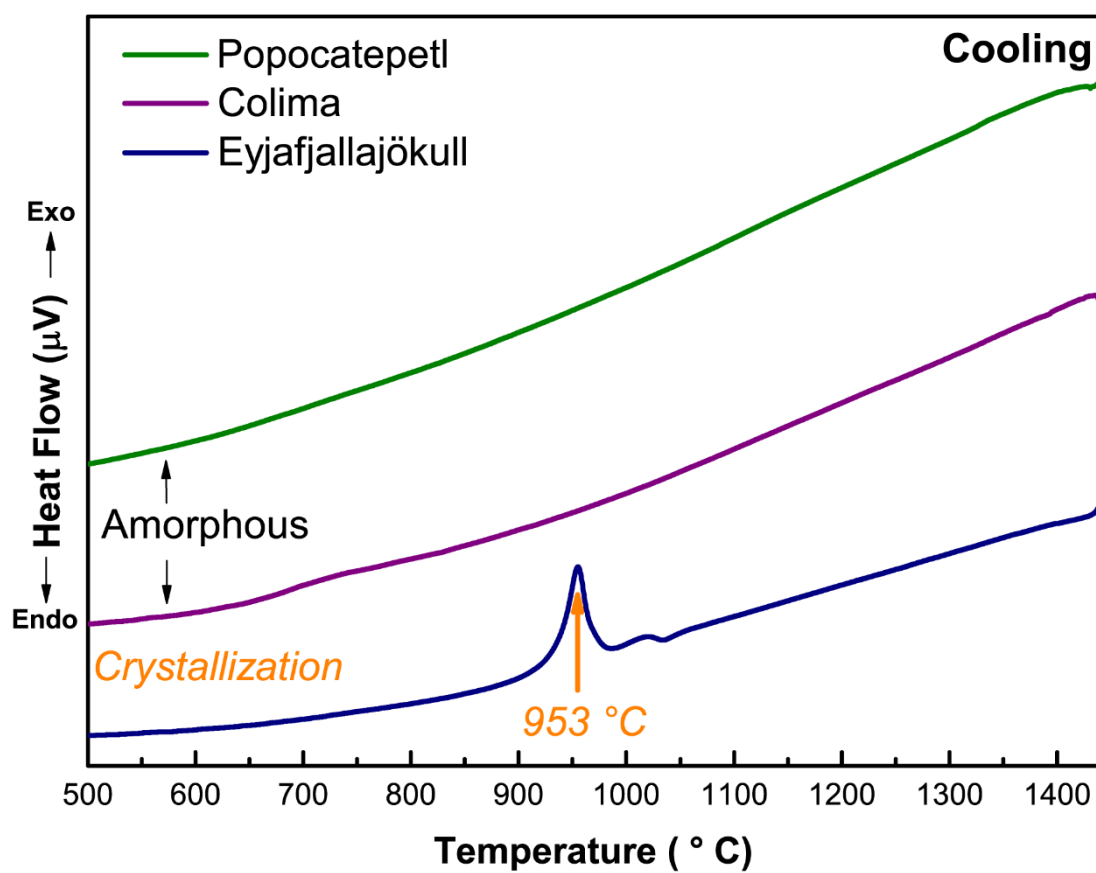


Figure 3.

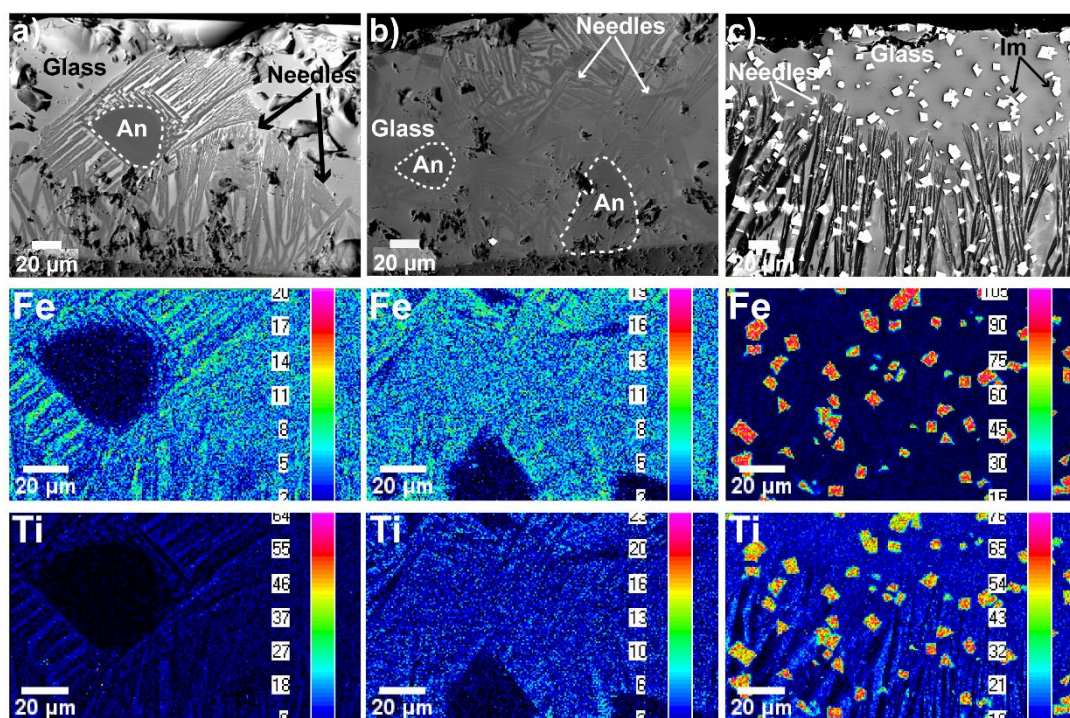


Figure 4.

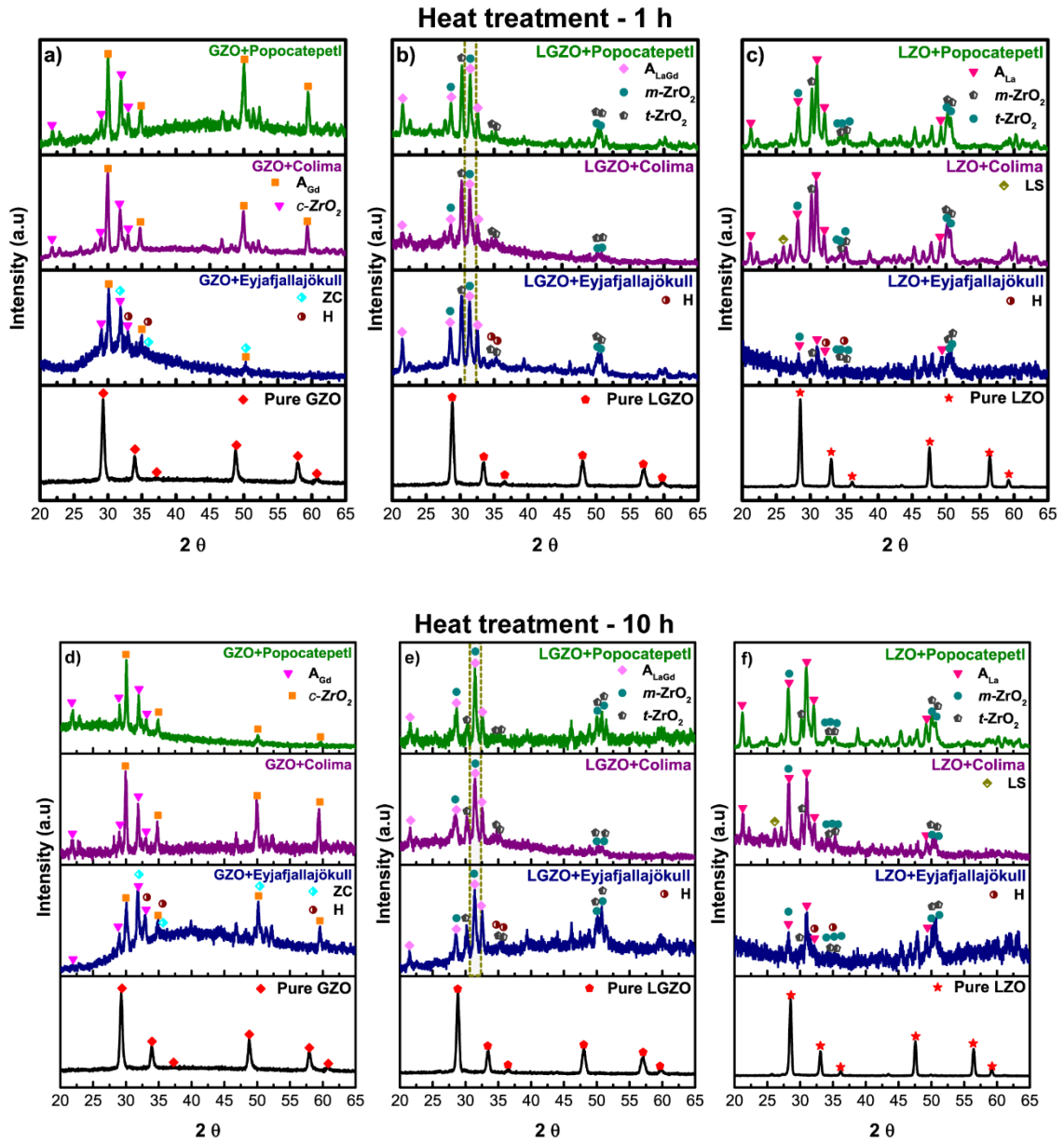




Figure 5.

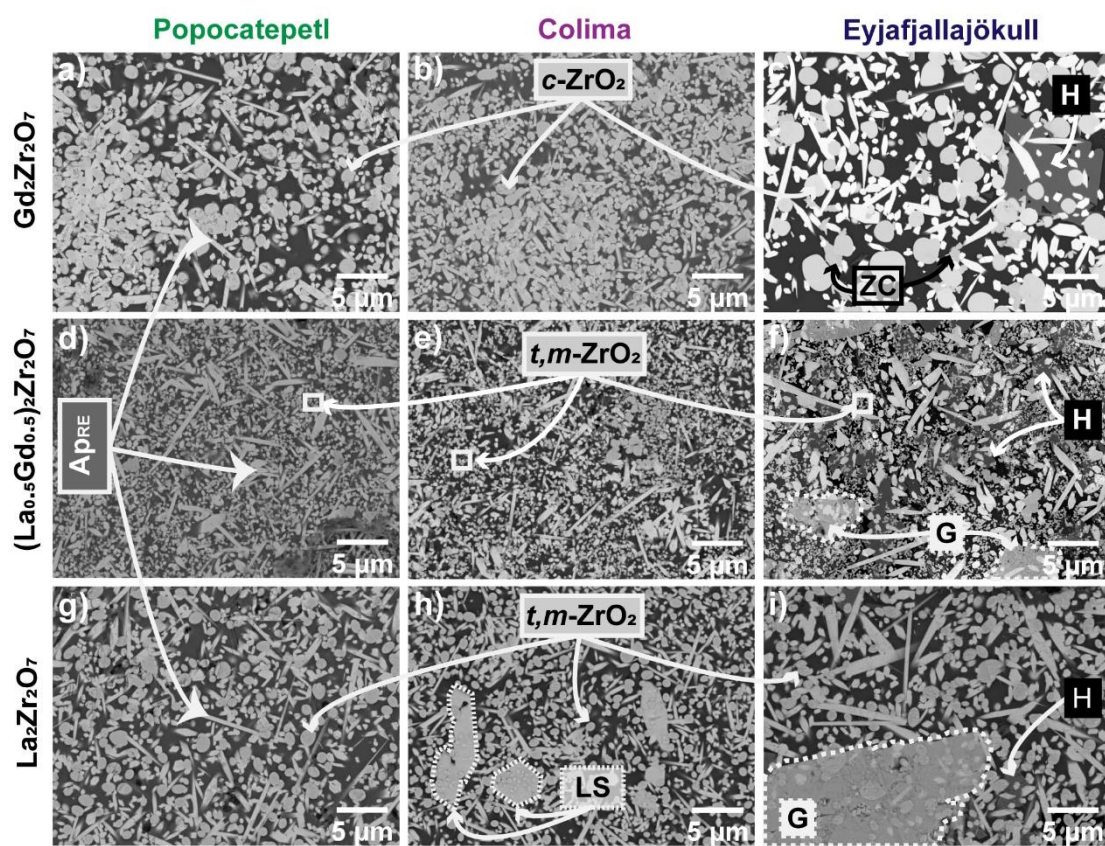


Figure 6.

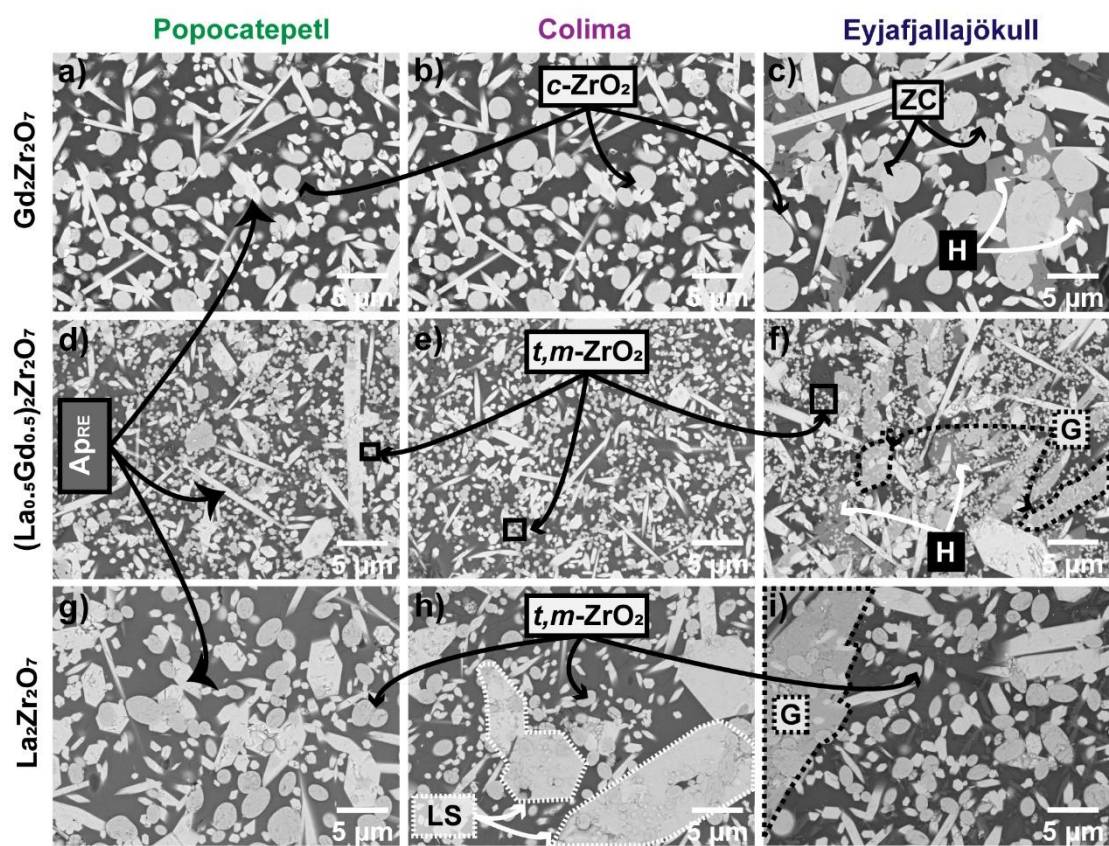


Figure 7.

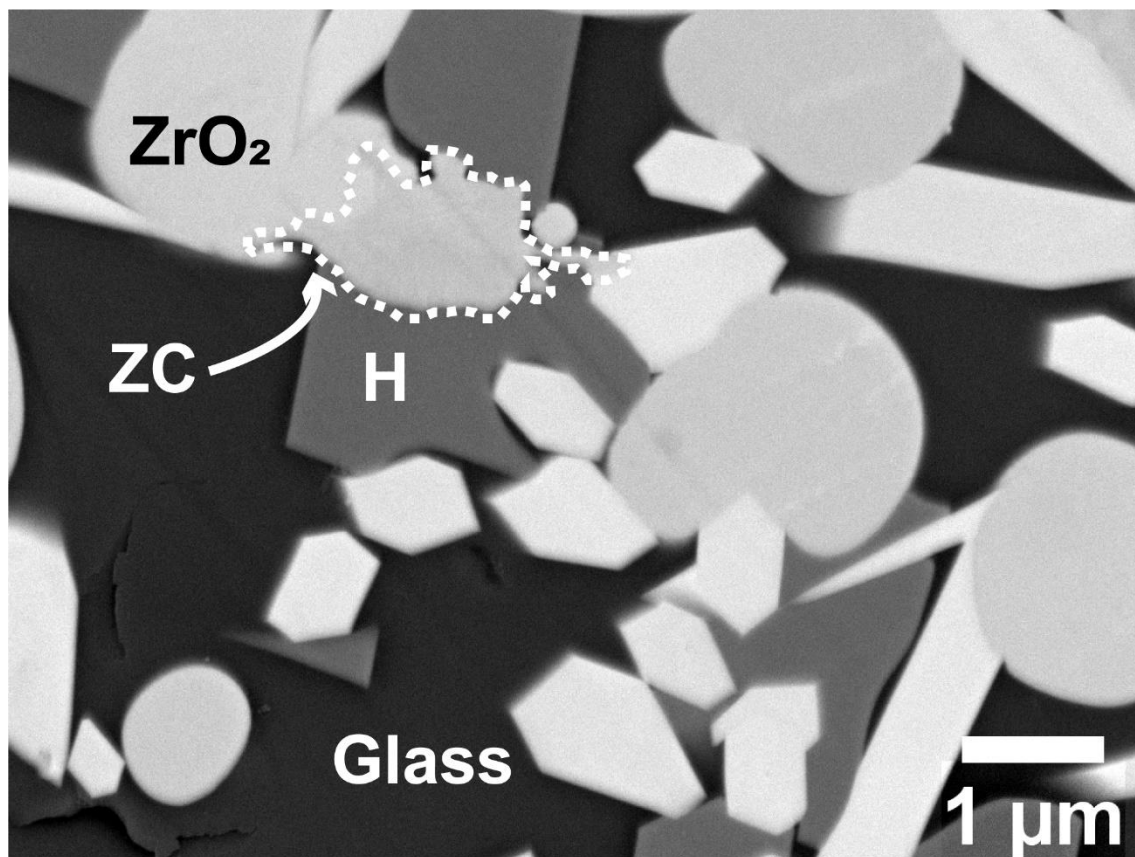


Figure 8.

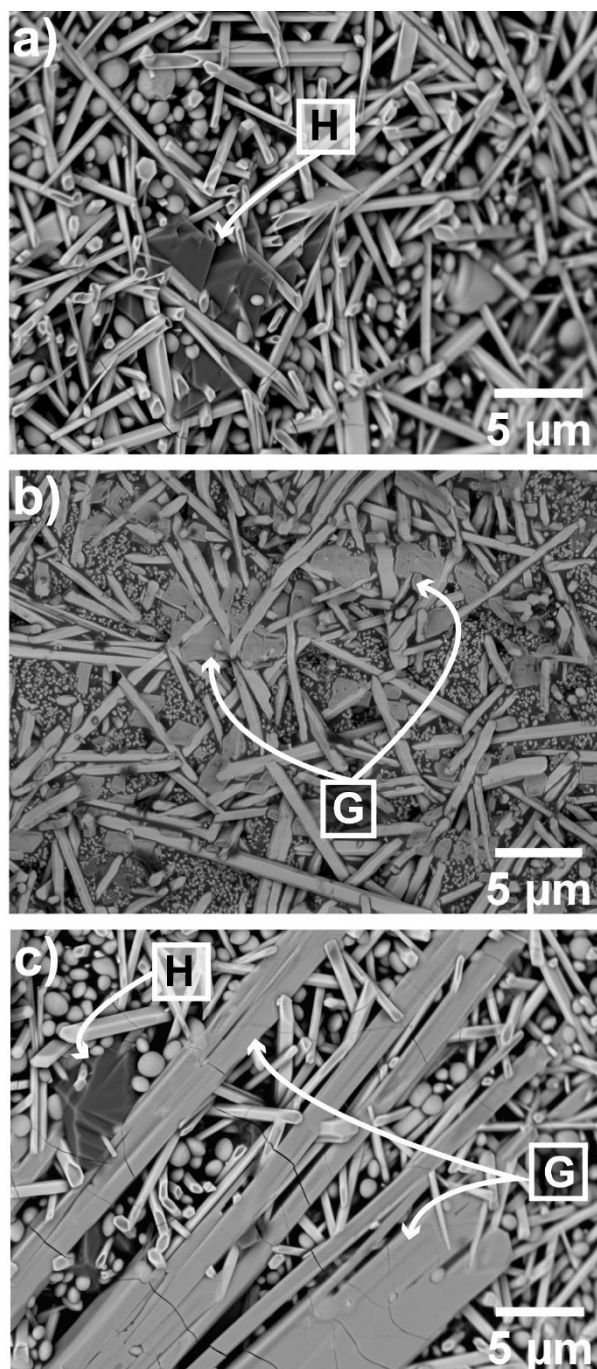




Figure 9.

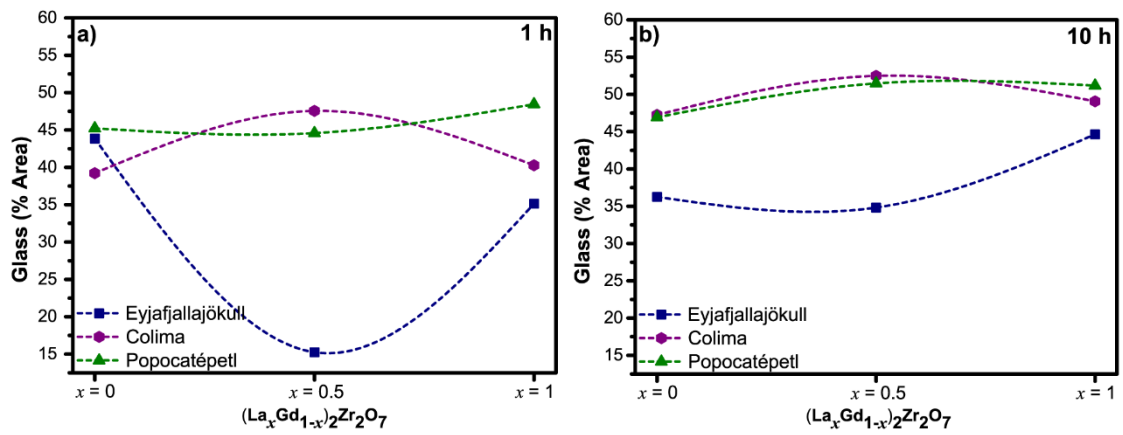


Figure 10.

